Enhanced microwave electromagnetic properties of core/shell/shell-structured Ni/SiO₂/PANI hexagonal nanoflake composites with preferred magnetization and polarization orientations

Jiaheng Wang [a,b], Siu Wing Or [a,*], Jun Tan [a,c]

[a] *Department of Electrical Engineering, The Hong Kong Polytechnic University, Hung Hom, Kowloon, Hong Kong*

[b] *Department of Mechanical Engineering, Hefei University of Technology, Xuancheng Campus, Anhui 242000, China*

[c] *Research Institute, Northeastern University, Shenyang 110004, China*

* Corresponding author. E-mail address: eeswor@polyu.edu.hk (S. W. Or)

ABSTRACT

Core/shell/shell-structured Ni/SiO₂/PANI hexagonal nanoflakes possessing in-plane [111] easy magnetization (*M*) and out-of-plane interfacial polarization (*P*) are synthesized by a three-step liquid chemical method, and their physicochemical properties and growth mechanism are investigated. Three characteristic types of paraffin-bonded ring-shaped nanoflake composites having random (R), vertical–horizontal (V–H), and horizontal–vertical (H–V) orientations of the orthogonal *M* and *P* to their two major surfaces are prepared by randomly, vertically, and horizontally aligning the nanoflakes in the paraffin matrix under a magnetic alignment and thermal curing process. The composites are evaluated experimentally and theoretically in the L–Ku (1–18 GHz) bands of microwaves in order to investigate the orientation effect of the orthogonal *M* and *P* on their microwave electromagnetic properties. The in-plane *M* in the H–V-oriented composite and the out-of-plane *P* in the V–H-oriented composite, which are parallel to the effective magnetic and electric field vectors of incident microwaves, result in a significant enhancement in permeability with multiple magnetic natural resonances and an obvious improvement in permittivity in comparison with other composites, respectively. The observations agree with the theoretical predictions based on the Landau–Lifshitz–Gilbert equation and Bruggeman's effective medium theory for permeability and the Debye's polarization theory for permittivity. As a result, the H–V-oriented composite achieves the best microwave electromagnetic impedance matching and absorption with a broad absorbing bandwidth of 4 GHz, a wide thickness range of 7–10 mm, and a minimal reflection loss of -41.5 dB in the Ku (12–18 GHz) band.

GRAPHICAL ABSTRACT
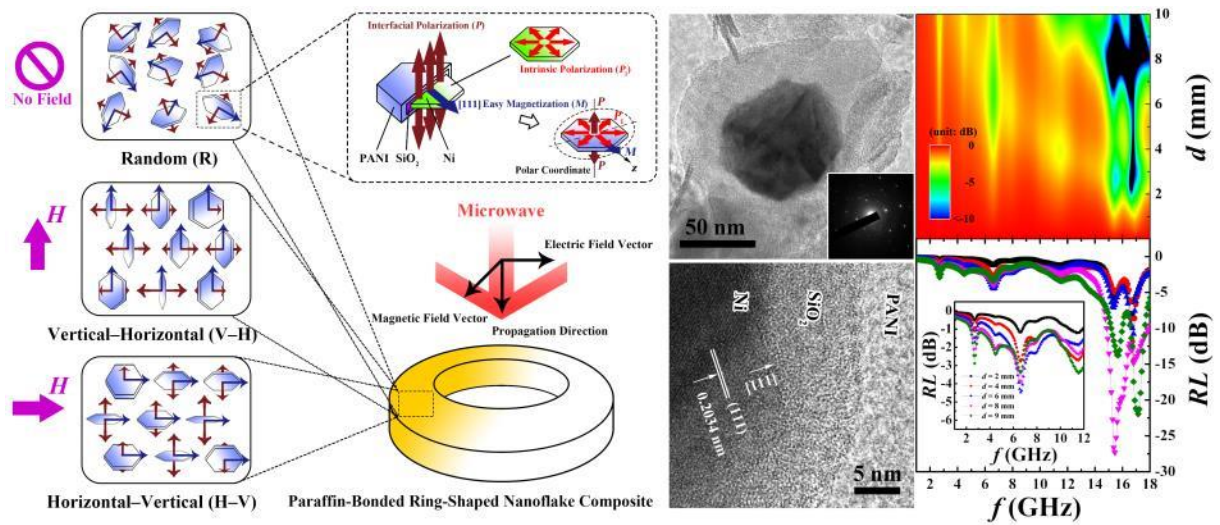
HIGHTLIGHTS

- Ni/SiO$_2$/PANI hexagonal nanoflakes with orthogonal in-plane magnetization (M) and out-of-plane polarization (P) are synthesized.

- Paraffin-bonded ring-shaped nanoflake composites with different orientations of the orthogonal M and P to surfaces are prepared.

- The orientation effect of the orthogonal M and P on the microwave electromagnetic properties is studied.

- The horizontal–vertical-oriented composite achieves the best microwave electromagnetic impedance matching and absorption.

Keywords:

Core/shell/shell structure; Hexagonal nanoflake composite; Impedance matching; Microwave electromagnetic properties; Orthogonal magnetization and polarization

1. Introduction

High-performance electromagnetic (EM) absorbers operating in the L–Ku (1–18 GHz) bands of microwaves are urgently needed to cope with the immediate and increasing challenges of EM radiation, interference, and compatibility caused by the rapid development and utilization of high-speed and high-frequency electronic and communication devices [1,2]. Core/shell-structured magnetic/dielectric nanospheres or nanoparticles, typically consisting of spherical magnetic cores coated by a layer of dielectric shell, both in nanometer size, have received considerable attention over the past decade as new generation microwave EM absorbers because of their unique ability to produce absorbers of smaller thickness and weight compared to the bulk and microscale counterparts [3–5]. However, the limited absorption at narrow absorbing bandwidth and absorber thickness range in the nanosphere-based absorbers have led to the development of core/shell- and core/shell/shell-structured nanoarchitectures and their absorbers in more recent years [6–8].

From a physical perspective, the use of nanoarchitectures (e.g., rods, disks, plates, flakes, etc.), in replacement of nanospheres, as the magnetic cores is capable of improving permeability and exceeding the Snoek's limit in the microwave frequency range via the contribution of shape anisotropy [6–10]. In fact, the isotropic nature of the spherical magnetic cores restricts intrinsically the permeability close to unity, which is far below the permittivity of the core/shell and core/shell/shell structures for establishing a good EM impedance matching at microwave frequencies. The addition of the 2nd shell is mainly aimed to increase the material-phase variety and flexibility for obtaining an EM impedance matching since the distinct dielectric properties of the conducting, semiconducting, and insulating dielectric shells will bring about characteristically different interfacial polarization effects, and hence microwave EM properties, in the resulting core/shell/shell structures [11–13].

Today, some core/shell- and core/shell/shell-structured nanoarchitectures have been synthesized and embedded in an EM-transparent bonding matrix to form composites showing improved microwave EM properties [6–8]. Nevertheless, there are three major deficiencies in the explication of the property improvement in relation to the magnetization and polarization designs of the architectural magnetic cores as well as their effects on the resulting composites. First, the reported architectural magnetic cores were mainly evolved from the spherical magnetic cores to induce shape-anisotropically enhanced permeability without intentionally designing and matching their shape anisotropy direction with easy magnetization direction or plane. Second, while shape anisotropy existed in the reported architectural magnetic cores, most composites were simply prepared by a random dispersion of the architectural magnetic

3

cores in the bonding matrix without any alignment of their shape anisotropy direction or even orientation of their easy magnetization direction or plane to match with the magnetic field vector of incident microwaves. Third, the intrinsic polarization associated with the architectural magnetic cores and the interfacial polarization induced by the core/shell or core/shell/shell structures have not been properly utilized to match with the electric field vector of incident microwaves.

Two-dimensional (2D) single-crystalline magnetic nanoarchitectures are great candidates as architectural magnetic cores for designing preferred magnetization and polarization directions because of their unique easy magnetization, anisotropic intrinsic polarization, and uniform interfacial polarization [14–16]. By designing and matching the induced shape anisotropy direction with the preferred magnetization and polarization directions in these 2D architectural magnetic cores as well as their core/shell- or core/shell/shell-structured nanoarchitectures, physically interesting composites possessing preferred magnetization and polarization orientations can be prepared by magnetically aligning the nanoarchitectures with respect to the magnetic and/or electric field vector(s) of incident microwaves during the curing of the bonding matrix.

In this paper, we propose an advanced type of core/shell/shell-structured nanoarchitecture, called $Ni/SiO_2/PANI$ hexagonal nanoflakes, which feature orthogonal in-plane [111] easy magnetization (M) and out-of-plane interfacial polarization (P) to match with the orthogonal magnetic and electric field vectors of microwaves. The magnetic core is a 2D single-crystalline Ni hexagonal nanoflake, which is specifically synthesized to impart shape-anisotropically induced in-plane M and intrinsic polarization (P_I). The double-shell is $SiO_2/PANI$, which is especially coated onto the Ni hexagonal nanoflake magnetic core to create the out-of-plane P. The 1st SiO_2 shell is an insulating dielectric shell to reduce the excessive permittivity of the Ni hexagonal nanoflake magnetic core and the 2nd PANI conducting dielectric shell for a better EM impedance matching. A magnetic alignment of the Ni hexagonal nanoflake magnetic core is performed to form paraffin-bonded ring-shaped nanoflake composites with three different M–P orientations in random (R), vertical–horizontal (V–H), and horizontal–vertical (H–V) directions. The physicochemical properties of the $Ni/SiO_2/PANI$ hexagonal nanoflakes are investigated, the growth mechanism of the Ni hexagonal nanoflake magnetic core is elucidated, and the microwave EM properties of the nanoflake composites are evaluated in the full L–Ku (1–18 GHz) microwave bands. The studies also include the theoretical analysis of the complex relative permeability of the composites using Landau-Liftshitz-Gilbert equation and Bruggerman's effective medium

theory as well as the complex relative permittivity using Debye's polarization theory. Finally, the magnetic and dielectric losses, impedance matching map, and reflection loss are determined to explain the orientation effect of the orthogonal M and P on the enhanced microwave EM properties.

2. Experimental details

2.1. Reagents used

All reagents for the synthesis of the core/shell/shell-structured Ni/SiO$_2$/PANI hexagonal nanoflakes were commercially acquired from Sinopharm Chemical Reagent Co., Ltd. and Aladdin Bio-Chem Technology Co., Ltd. in China. They were of analytical or certified American Chemical Society (ACS) grade and were used without any further purification. Nickel chloride anhydrous (NiCl$_2$), sodium dodecyl sulfate (SDS), sodium hydroxide (NaOH), and sodium hypophosphite (NaH$_2$PO$_2$) were employed for preparing the Ni hexagonal nanoflake magnetic core. Anhydrous ethanol (C$_2$H$_5$OH), ammonium hydroxide (NH$_4$OH), and tetraethyl orthosilicate (TEOS) were selected for coating the 1st SiO$_2$ insulating dielectric shell. SDS, ammonium persulfate ((NH$_4$)$_2$S$_2$O$_8$), hydrochloric acid (HCl) of 37%, and aniline (C$_6$H$_7$N) were chosen for coating the 2nd PANI conducting dielectric shell. Polyvinylpyrrolidone (PVP) K30 was adopted for modifying the core/shell/shell interfaces. Ultrapure 18.2 MΩ·cm water (H$_2$O) delivered by a water purification system (Thermo Scientific Barnstead 50132366 MicroPure) was used as the solvent throughout the whole synthesis process.

2.2. Synthesis of Ni/SiO$_2$/PANI hexagonal nanoflakes

The Ni/SiO$_2$/PANI hexagonal nanoflakes were synthesized by a three-step liquid chemical process using the reagents stated in Section 2.1. First, the 2D single-crystalline Ni hexagonal nanoflake magnetic core was prepared using a surfactant-assisted hydrothermal method [17]. In a typical reaction, NiCl$_2$ of 1.5 mmol and SDS of 0.45 mmol were dissolved in ultrapure water of 20 mL under magnetic stirring. NaOH of 10 mL, in a concentration of 3 mol/L, was rapidly added into the NiCl$_2$–SDS solution under continuous stirring until Ni^{2+} was completely precipitated. NaH$_2$PO$_2$ was introduced into the Ni^{2+}-precipitated solution to form a reductive precursor. The precursor was transferred into a Teflon-lined stainless steel autoclave before being heated in an oven at 110 ℃ for 14 h. After natural cooling to room

temperature, the Ni product was separated magnetically and washed ultrasonically by ethanol and ultrapure water for several times.

Second, the 1st SiO₂ insulating dielectric shell was coated on the as-prepared Ni product using a modified stöber method [18,19]. PVP of 1 g was dissolved in ultrapure water of 100 mL. The as-prepared Ni product was dispersed in the PVP solution and pretreated ultrasonically for 2 h to decorate the interface for SiO₂ coating. The interface-decorated Ni product was separated magnetically and re-dispersed homogeneously in a solution containing C₂H₅OH of 20 mL, NH₄OH of 0.5 mL, and ultrapure water of 5 mL. TEOS of 0.2 mL was injected slowly into the solution using a microsyringe under mechanical stirring for 20 h. The Ni/SiO₂ product was washed ultrasonically by ethanol and ultrapure water for several times, separated magnetically, and dispersed into ultrapure water of 100 mL.

Third, the 2nd PANI conducting dielectric shell was coated on the as-prepared Ni/SiO₂ product using an in-situ polymerization method [20]. The PVP pretreatment used for coating the 1st SiO₂ insulating dielectric shell described above was also applied to the Ni/SiO₂ product for decorating the interface for PANI coating. The interface-decorated Ni/SiO₂ product was separated magnetically and dispersed in a solution containing SDS of 0.08 g, (NH₄)₂S₂O₈ of 0.01 g, HCl of 3 mL, and ultrapure water of 10 mL under mechanical stirring. C₆H₇N of 8 μL was injected slowly into the solution using a micropipettor under mechanical stirring for 8 h in an ice-water bath. The Ni/SiO₂/PANI product was washed ultrasonically by ethanol and ultrapure water for several times, separated magnetically, and dried in a vacuum oven at 60 ℃ for 24 h.

2.3. Preparation of paraffin-bonded ring-shaped nanoflake composites

Fig. 1 shows the schematic diagram of three characteristic types of paraffin-bonded ring-shaped nanoflake composites. They feature random (R), vertical–horizontal (V–H), and horizontal–vertical (H–V) orientations of the orthogonal in-plane [111] easy magnetization (*M*) (marked with blue arrows) and out-of-plane interfacial polarization (*P*) (marked with brown arrows) of the Ni/SiO₂/PANI hexagonal nanoflakes to their two major surfaces under a DC magnetic alignment field (*H*) (marked with big pink arrows) during the thermal curing of the paraffin matrix (not shown). The inset at the upper right corner illustrates the details of the core/shell/shell structure, together with the magnetization and polarization directions, of a Ni/SiO₂/PANI hexagonal nanoflake. Each nanoflake has shape-anisotropically induced in-plane *M* and intrinsic polarization (*P*I) (marked with red arrows), besides a Ni/SiO₂/PANI interface-induced out-of-plane *P*. The orthogonal in-plane *M* and out-of-plane *P* are arranged

in the polar coordinate system. The orthogonality of the propagation direction, electric field vector, and magnetic field vector of a microwave is also shown.

The three types of paraffin-bonded ring-shaped nanoflake composites in Fig. 1 were prepared by dispersing 40 wt% Ni/SiO$_2$/PANI hexagonal nanoflakes in a ring-shaped nonmagnetic brass mold (3.04 mm inner diameter, 7 mm outer diameter, and 2 mm thickness) containing an EM-transparent paraffin bonding matrix (48–50 ºC melting point). For ease of description, the nanoflake composites with R, V–H, and H–V orientations of the orthogonal M and P to their two major surfaces are denoted as the R-, V–H-, and H–V-orientated composites, respectively. The V–H- and H–V-orientated composites were formed by applying a DC magnetic alignment field (H) of 1 T to the vertical (or perpendicular) and horizontal (or parallel) directions of the two major surfaces of the ring-shaped nonmagnetic brass mold, respectively, in a temperature-controlled chamber at 60 ºC for 2 h. H was not required for preparing the R-oriented composite.
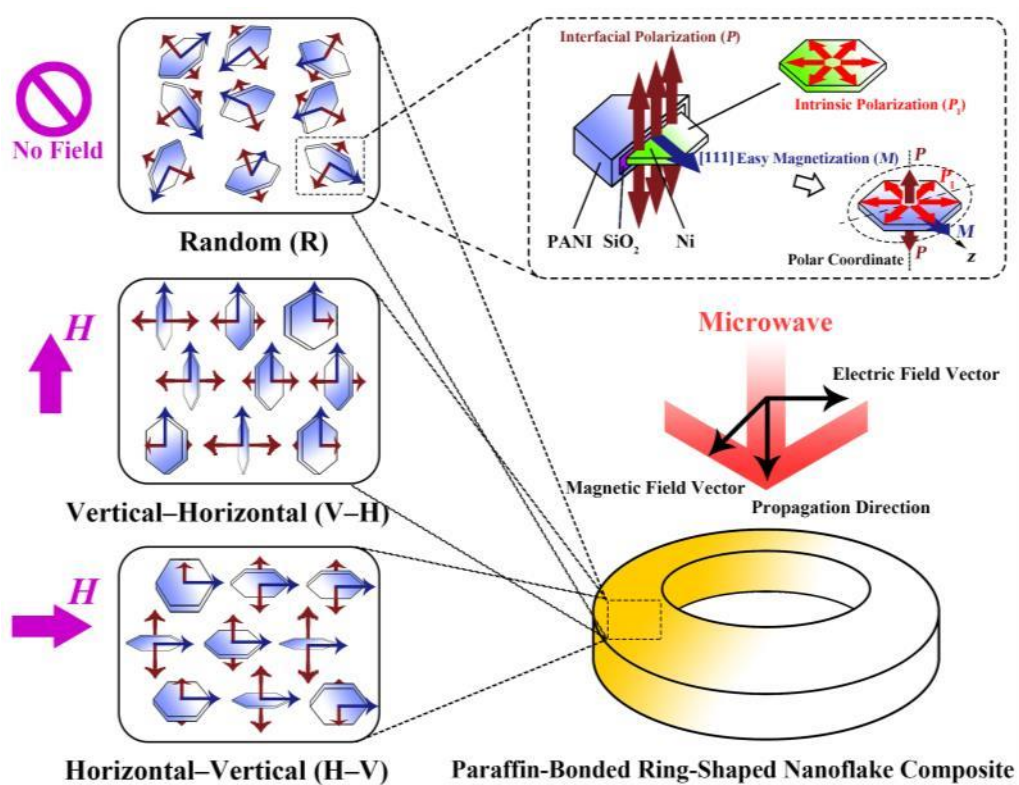

Fig. 1 Schematic diagram of paraffin-bonded ring-shaped nanoflake composites with random (R), vertical–horizontal (V–H), and horizontal–vertical (H–V) orientations of the orthogonal in-plane [111] easy magnetization (M) and out-of-plane interfacial polarization (P) of Ni/SiO$_2$/PANI hexagonal nanoflakes to their two major surfaces under a magnetic alignment field H during thermal curing of paraffin matrix. The inset at the upper right corner illustrates a Ni/SiO$_2$/PANI hexagonal nanoflake having shape-anisotropically induced in-plane M and intrinsic polarization (P_I), besides a Ni/SiO$_2$/PANI interface-induced out-of-plane P. The orthogonality of propagation direction, electric field vector, and magnetic field vector of a microwave is also shown.

2.4. Evaluation of physicochemical and microwave electromagnetic properties

The crystal phase of the as-prepared Ni and Ni/SiO$_2$/PANI products was analyzed by an X-ray diffractometer (XRD, Rigaku SmartLab) with a rotating anode X-ray tube of Cu-$K\alpha$ radiation (λ=1.54 Å) at a θ–2θ scan rate of 4°/min. The morphology and nanostructure of both products were investigated by a transmission electron microscope (TEM, JEOL JEM-2100F) at an emission voltage of 200 kV. The high-resolution interface morphology and crystal orientation of both products were examined by a Cs-corrected scanning transmission electron microscope (STEM, JEOL JEM-ARM200F) with a cold field emission gun at an acceleration voltage of 200 kV. The samples for TEM and STEM evaluations were prepared by applying one droplet of the suspension (1 mg per 3 ml) of ethanol and Ni or Ni/SiO$_2$/PANI product onto a holey carbon film-covered copper microgrid. The elemental valence states of the Ni/SiO$_2$/PANI product were investigated by an X-ray photoelectron spectroscope (XPS, Thermo Fisher Scientific ESCALAB250Xi) with a monochromatic X-ray source (an Al-$K\alpha$ line of 1486.6 eV) at a spot size of 500 μm and a pass energy of 30 eV. The chemical bond vibrations of both products were detected by a Fourier-transform infrared (FTIR) spectroscope (Agilent Cary 630) with an attenuated total reflectance accessory. The Raman spectra of both products were inspected by a Raman spectrometer (HORIBA JOBIN YVON LabRam HR Evolution) with a laser excitation of 532 nm at room temperature.

The scattering (S-) parameters of the nanoflake composites were measured at different thicknesses (d) by a transmission/reflection coaxial line method in the 1–18 GHz frequency (f) range (i.e., the L–Ku bands of microwaves) using a computer-controlled microwave network analyzer (Keysight PNA-X N5244A). The microwave network analyzer was first calibrated by a standard mechanical calibration kit (Keysight 85050D) from DC to 18 GHz, and the nanoflake composite to be measured was inserted into an airline holder (Keysight 85051BR03) having a ring-shaped cavity of 3.04 mm inner diameter, 7 mm outer diameter, and 99.898 mm depth. The f dependence of complex relative permeability ($\mu_r = \mu_r' - j\mu_r''$) and complex relative permittivity ($\varepsilon_r = \varepsilon_r' - j\varepsilon_r''$) at various d were determined by a materials measurement software suite (Keysight N1500A) preinstalled in the computer on the basis of the measured S-parameter responses and the Nicolson-Ross-Weir method [21,22]. The f dependence of reflection loss (RL) at various d was deduced from the determined μ_r and ε_r spectra using [6,7]:

$$RL = 20 \log |(Z_{in} - 1)/(Z_{in} + 1)| \tag{1}$$

$$Z_{\text{in}} = \sqrt{\frac{\mu_r}{\varepsilon_r}} \tanh\left(j\frac{2\pi f d}{c}\sqrt{\mu_r \varepsilon_r}\right) \qquad (2)$$

where Z_{in} is the normalized input impedance of nanoflake composite, j is the unit imaginary number, and $c=3\times10^8$ m/s is the velocity of light.

3. Results and discussion

3.1. *Physicochemical properties* of Ni/SiO₂/PANI hexagonal nanoflakes

Fig. 2 shows the XRD θ–2θ scanning patterns of typical Ni and Ni/SiO$_2$/PANI products. Three diffraction peaks are clearly seen in both products at three different 2θ values of 44.5º, 51.8º, and 76.4º. These diffraction peaks can be assigned, respectively, to the (111), (200), and (220) planes of a typical face-centered cubic (fcc) phase of Ni (*Fm-3m*) in accordance with JCPDS No. 04-0850. No diffraction peaks in relation to other impurities such as Ni oxides are detected in both products. This implies the existence of a sufficiently high purity in the Ni crystal state of both products. For the Ni/SiO$_2$/PANI product, this further hints at a good oxidation protection of the Ni core by the SiO$_2$ and PANI shells. The reason why no diffraction peaks are detected for the SiO$_2$ and PANI shells is mainly due to their amorphous state after being synthesized by the modified stöber method and the in-situ polymerization method in Section 2.2, respectively.
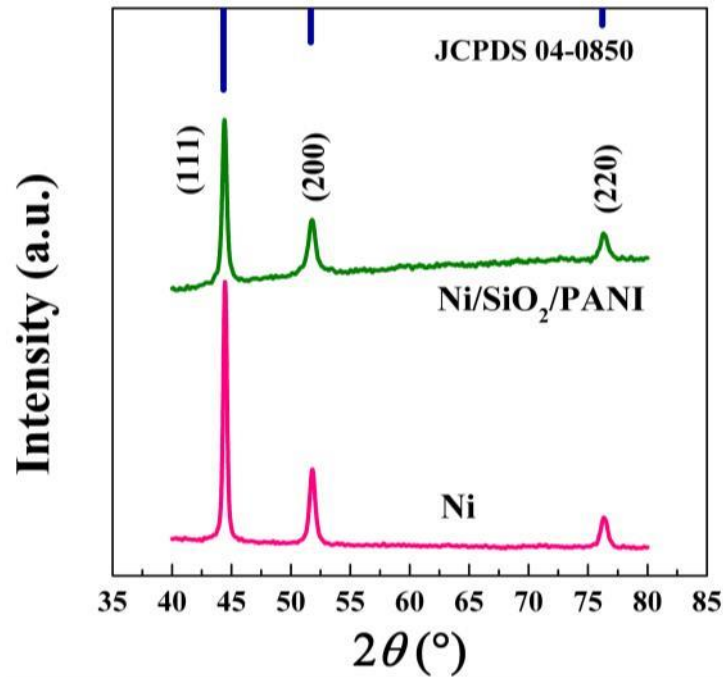

Fig. 2 XRD θ–2θ scanning patterns of typical Ni and Ni/SiO₂/PANI products.

Fig. 3(a) shows the TEM image of a typical Ni product. The Ni product has a 2D uniform flake-shaped morphology in forms of hexagonal nanoflakes with a darker contrast and quasi-hexagonal nanoflakes with a lighter contrast. The hexagonal nanoflakes have a size of 70–100 nm and a thickness of 8–15 nm, while the quasi-hexagonal ones are relatively smaller in both size (50–80 nm) and thickness (3–4 nm). These quasi-hexagonal nanoflakes are the residual embryonic crystallites of the hexagonal nanoflakes as a result of an insufficient growth during the precipitation process (Section 2.2). The growth of the hexagonal nanoflakes will be described in Section 3.2. Fig. 3(b) illustrates the magnified TEM image of a typical hexagonal nanoflake. It is clear that the two major surfaces of the hexagonal nanoflake are in hexagonal shape, and these hexagonal surfaces are the easy magnetization planes because of shape anisotropy. The selected area electron diffraction (SAED) pattern in the inset exhibits a set of symmetric diffraction spots including the (111) plane of Ni. This infers the existence of a single-crystalline state and an in-plane [111] easy magnetization direction in the hexagonal nanoflake. Fig. 3(c) gives the HRTEM image of a typical hexagonal nanoflake acquired by STEM. The periodic lattice stripes with a lattice plane spacing of 0.2034 nm indicate the (111) plane of Ni. Since the direction perpendicular to the (111) plane is the [111] direction of Ni, and as the [111] direction of Ni is along the long axis of the hexagonal nanoflake surfaces, the [111] direction of Ni is thus the in-plane [111] easy magnetization direction of the hexagonal nanoflake. Fig. 3(d) displays the magnified TEM image of some typical quasi-hexagonal nanoflakes (upper), together with their HRTEM image (lower left) and fast Fourier transformation (FFT) pattern (lower right) obtained by STEM in the region marked by the blue rectangle on the magnified TEM image. The HRTEM image shows obvious periodic lattice stripes of 0.2034 nm lattice plane spacing featured by the (111) plane of Ni. The observation agrees well with that in Fig. 3(c) for the hexagonal nanoflake and suggests an in-plane [111] easy magnetization direction along the long axis of the quasi-hexagonal nanoflake surfaces. The FFT pattern demonstrates a set of symmetric diffraction spots, implying the single-crystalline state of the quasi-hexagonal nanoflakes. Therefore, the quasi-hexagonal nanoflakes are the embryos of the hexagonal nanoflakes with the same magnetization behavior.
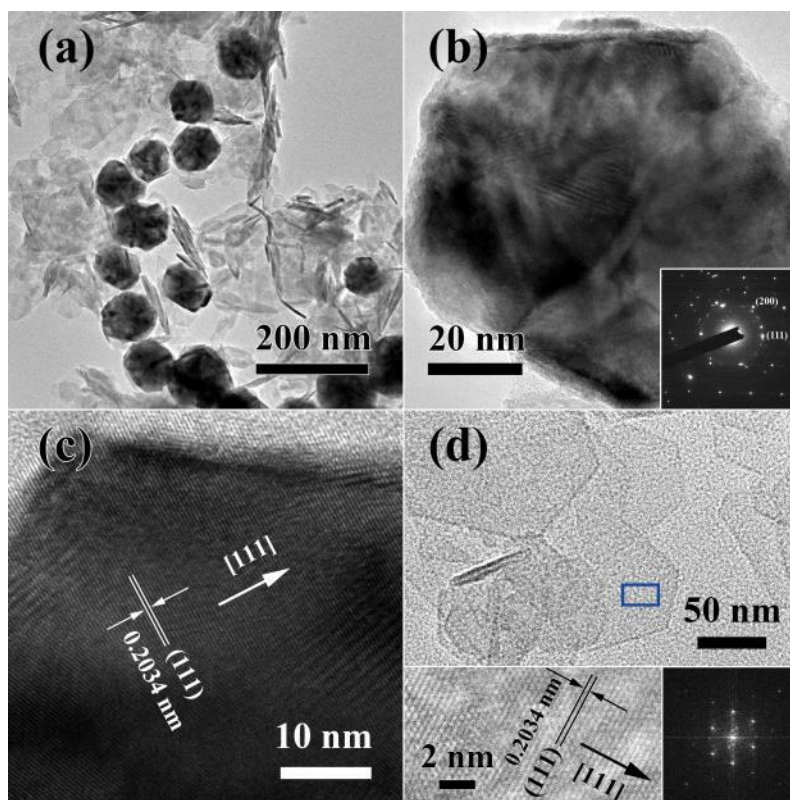
Fig. 3 (a) TEM image of a typical Ni product, showing a 2D uniform flake-shaped morphology in forms of hexagonal nanoflakes (darker contrast) and quasi-hexagonal nanoflakes (lighter contrast); (b) Magnified TEM image of a typical hexagonal nanoflake with its SAED pattern in the inset; (c) HRTEM image of a typical hexagonal nanoflake acquired by STEM; (d) Magnified TEM image of some typical quasi-hexagonal nanoflakes (upper) with their HRTEM image (lower left) and FFT pattern (lower right) obtained by STEM in the region marked by blue rectangle.

Fig. 4(a) shows the TEM image of a typical Ni/SiO$_2$/PANI product. The Ni/SiO$_2$/PANI product has the 2D single-crystalline Ni hexagonal and quasi-hexagonal nanoflakes discussed in Fig. 3 as the magnetic core coated by the SiO$_2$ and PANI shells with a lighter contrast. Fig. 4(b) illustrates the magnified TEM image of a typical Ni/SiO$_2$/PANI hexagonal nanoflake. It is obvious that the Ni hexagonal nanoflake magnetic core with a darker contrast remains in hexagonal shape as in Fig. 3(b), while the SiO$_2$ and PANI shells have a total thickness of 20–50 nm. The SAED pattern in the inset consists of symmetric diffraction spots and concentric broad rings so that the Ni hexagonal nanoflake magnetic core is in a single-crystalline state and the SiO$_2$ and PANI shells are in an amorphous state. Fig. 4(c) gives the HRTEM image of a typical Ni/SiO$_2$/PANI hexagonal nanoflake acquired by STEM. A typical core/shell/shell structure is clearly seen for the Ni hexagonal nanoflake magnetic core, the 1st SiO$_2$ insulating dielectric shell, and the 2nd PANI conducting dielectric shell. The periodic lattice stripes with a lattice plane spacing of 0.2034 nm in the Ni hexagonal nanoflake magnetic core, in a good agreement with Fig. 3(c), suggest the (111) plane of Ni and an in-plane [111] direction of Ni

along the long axis of the Ni hexagonal nanoflake magnetic core surfaces. The 1st SiO_2 insulating dielectric shell and the 2nd PANI conducting dielectric shell, owing to their different contrasts, can be easily distinguished to have different thicknesses of 7–10 and 13–40 nm, respectively. Fig. 4(d) provides the magnified TEM image of some typical Ni/SiO$_2$/PANI quasi-hexagonal nanoflakes (upper), together with their HRTEM image (lower left) and SAED pattern (lower right) obtained by STEM in the region marked by the blue rectangle on the magnified TEM image. From the HRTEM image, the periodic lattice stripes of 0.2034 nm lattice plane spacing featured by the (111) plane of Ni in the Ni hexagonal nanoflake magnetic core (Fig. 4(c)) is also observed in these Ni quasi-hexagonal nanoflake magnetic cores. Thus, the in-plane [111] easy magnetization direction is along the long axis of the Ni quasi-hexagonal nanoflake magnetic core surfaces. From the SAED pattern, the satellite diffraction spots and the broad rings reflect the overlapping of several single-crystalline thin Ni quasi-hexagonal nanoflake magnetic cores and amorphous SiO_2 and PANI shells, respectively.
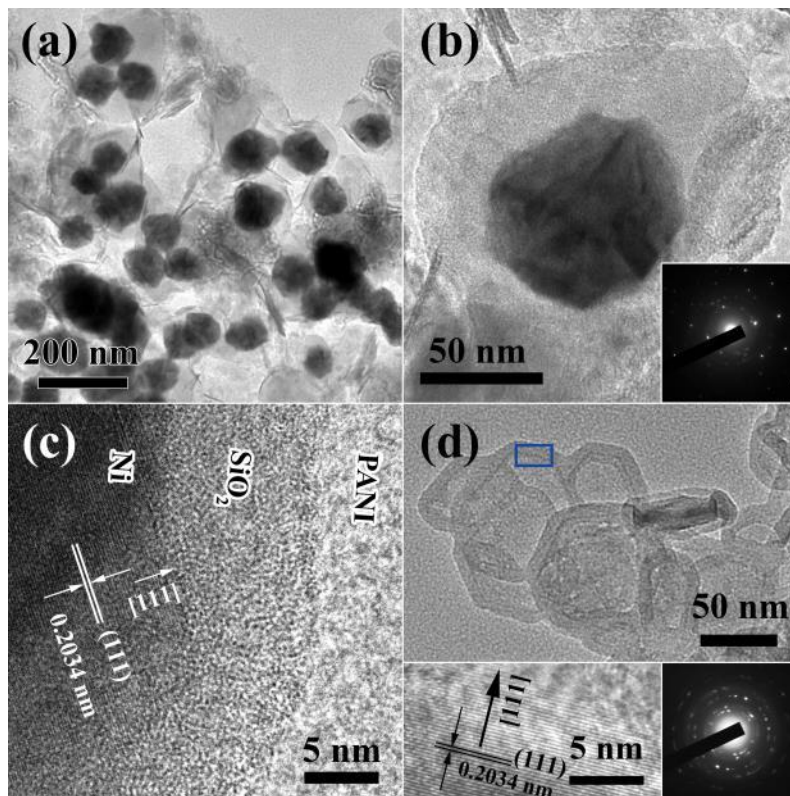

Fig. 4 (a) TEM image of a typical Ni/SiO$_2$/PANI product; (b) Magnified TEM image of a typical Ni/SiO$_2$/PANI hexagonal nanoflake with its SAED pattern in the inset; (c) HRTEM image of a typical Ni/SiO$_2$/PANI hexagonal nanoflake acquired by STEM; and (d) Magnified TEM image of some typical Ni/SiO$_2$/PANI quasi-hexagonal nanoflakes (upper) with their HRTEM image (lower left) and SAED pattern (lower right) obtained by STEM in the region marked by blue rectangle.

Fig. 5 shows a typical XPS survey spectrum of the Ni/SiO$_2$/PANI hexagonal nanoflakes in the binding energy range of 0–1350 eV. All the contained elements were carefully scanned in their typical Ni 2p, O 1s, N 1s, C 1s, and Si 2p regions, and the corresponding spectra are illustrated as the insets. All the XPS peaks can be indexed to the elements of Ni, O, N, C, and Si constituted by the Ni hexagonal nanoflake magnetic core, the 1st SiO$_2$ insulating dielectric shell, and the 2nd PANI conducting dielectric shell of the Ni/SiO$_2$/PANI hexagonal nanoflakes [23,24]. The pair of XPS peaks at 873 and 855 eV, corresponding to the Ni 2p$_{1/2}$ and 2p$_{3/2}$, respectively, indicates the existence of zero charge state of Ni element in the Ni hexagonal nanoflake magnetic core. The two individual XPS peaks at 532 and 103 eV, corresponding to the O 1s and the Si 2p (i.e., Si^{4+} 2p$_{3/2}$ [24]), respectively, suggest the presence of the 1st SiO$_2$ insulating dielectric shell. The N 1s peak and the C 1s peak at 399 and 285 eV mean the benzenoid ring and the imino group in the 2nd PANI conducting dielectric shell, respectively.
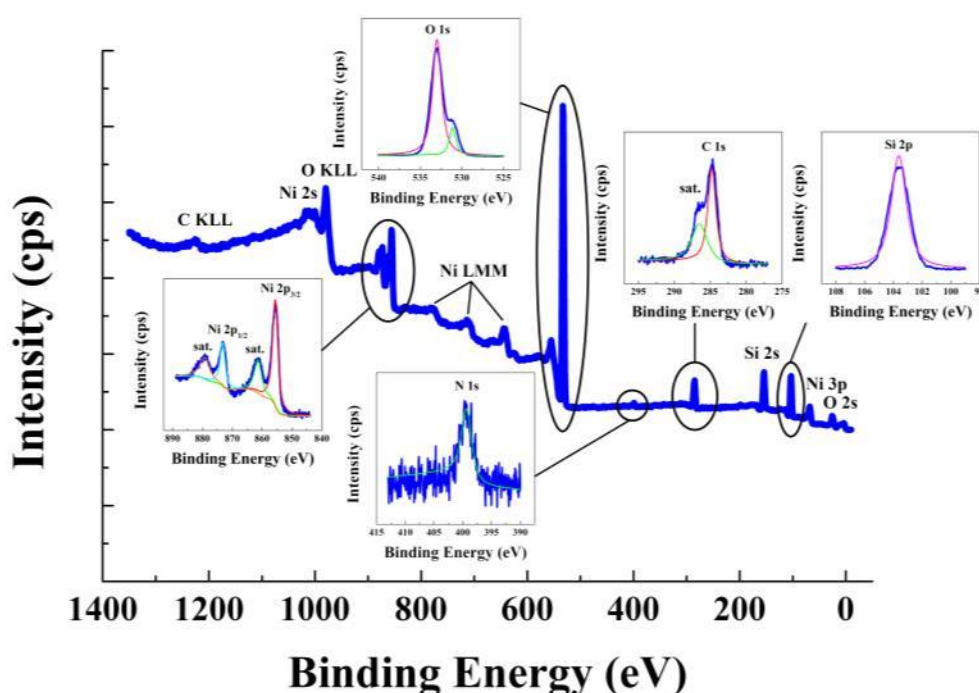

Fig. 5 XPS survey spectrum of Ni/SiO$_2$/PANI hexagonal nanoflakes. The insets are scanned spectra in typical Ni 2p, O 1s, N 1s, C 1s, and Si 2p regions.

Fig. 6(a) shows the FTIR spectra of the Ni/SiO$_2$/PANI hexagonal nanoflakes and their Ni hexagonal nanoflake magnetic cores. The Ni/SiO$_2$/PANI hexagonal nanoflakes and the Ni hexagonal nanoflake magnetic cores have two common peaks at 514 and 462 cm^{-1} because of the vibration of Ni. Other than these, the Ni/SiO$_2$/PANI hexagonal nanoflakes own 7 new peaks at 3640, 1636, 1490, 1304, 1080, 957, and 790 cm^{-1} in comparison with their Ni

hexagonal nanoflake magnetic cores. The 1st peak at 3640 cm^{-1} is the N–H stretching vibration of aromatic amines. The 2nd and 3rd peaks at 1636 and 1490 cm^{-1} are the C–N and C=C stretching vibrations of the benzenoid and quinoid rings, respectively. They are the characteristic vibrations of the nitrogen benzenoid and quinoid formed in a polymer with conducting state (e.g., PANI). The 4th peak at 1304 cm^{-1} belongs to the asymmetric C–N stretching vibration of the benzenoid ring. The 5th and 6th peaks at 1080 and 957 cm^{-1} are the peaks of the –N–quinoid–N– stretching vibrations. The 7th peak at 790 cm^{-1} is the C–H out-of-plane bending vibration of the substituted aromatic ring [25,26]. The above characteristic vibrations indicate the proper synthesis of the 2nd PANI conducting dielectric shell in the Ni/SiO$_2$/PANI hexagonal nanoflakes. Fig. 6(b) plots the Raman spectra of the Ni/SiO$_2$/PANI hexagonal nanoflakes and their Ni hexagonal nanoflake magnetic cores. There are 6 obvious peaks in the Ni/SiO$_2$/PANI hexagonal nanoflakes. The peaks at 1169, 1321, and 1383 cm^{-1} are assigned to the radical cations with vibrations of $\beta_{C–N}$ and $\upsilon_{C–N}$, while those at 1490 and 1591 cm^{-1} are indexed to the dications with vibrations of $\upsilon_{C=N}$ and $\upsilon_{C=C}$. The peak at 1224 cm^{-1} is for the benzenoid units with vibration of $\upsilon_{C–N}$ [27,28]. These characteristic vibrations imply that the 2nd PANI conducting dielectric shell is in an emeraldine structure. As the 1st SiO$_2$ insulting dielectric shell is not sensitive to both FTIR and Raman, no peaks are detected.
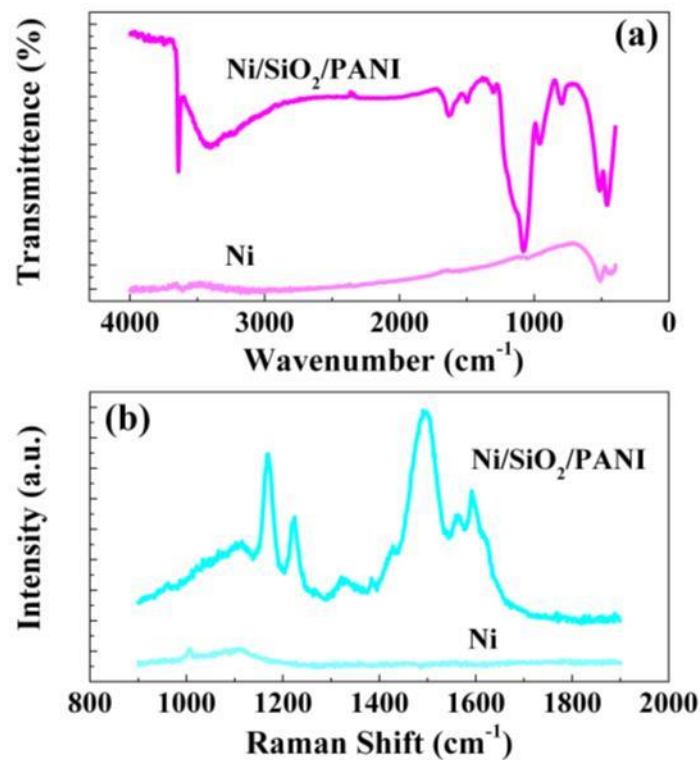

Fig. 6 (a) FTIR and (b) Raman spectra of Ni hexagonal nanoflakes and Ni/SiO$_2$/PANI hexagonal nanoflakes.

3.2 Growth mechanism of Ni hexagonal nanoflakes

The growth of a magnetic metal always tends to form a spherical shape with the same growth speed in all directions [29,30]. In the present work, we utilize a highly repeatable surfactant-assisted hydrothermal method to prepare the 2D single-crystalline Ni hexagonal nanoflake magnetic cores in Fig. 3(b) using $Ni(OH)_2$ as the template and SDS as the surfactant [17]. With the dissolution of $NiCl_2$ and SDS in ultrapure water, a solution of Ni^{2+} and SDS is generated. By rapidly adding NaOH into the solution, Ni^{2+} will react with OH^- to form $Ni(OH)_2$ precipitation, which is easier to form a flake shape [31]. As an anionic surfactant, SDS in the Ni^{2+}-precipitated solution will adsorb on the major surfaces of the $Ni(OH)_2$ flakes and prevent them from further reactions. By introducing NaH_2PO_2 into the Ni^{2+}-precipitated solution to form a reductive precursor, the $Ni(OH)_2$ flakes will go through a reduced chemical reaction to form Ni hexagonal nanoflakes described by the following chemical formula:

$$Ni^{2+} + H_2PO_2^- + H_2O \rightarrow Ni + H_2PO_3^- + 2H^+$$

where NaH_2PO_2 is the reduction reagent [32]. During the reduced chemical reaction, the strong alkaline solution will promote the reduction of the Ni embryos from the $Ni(OH)_2$ flakes to the Ni quasi-hexagonal nanoflakes (Figs. 3(d) and 7). In the meantime, the adsorbing of the SDS ions on the $Ni(OH)_2$ flakes will poison the dangling bonds of Ni, thereby inhibiting the growth perpendicular to the 2D major surfaces of the Ni quasi-hexagonal nanoflakes. Under the continuous hydrothermal heating, the Ni quasi-hexagonal nanoflakes will keep growth along the 2D major surfaces and form the desired Ni hexagonal nanoflakes (Figs. 3(b) and 7). Since the concentration of $Ni(OH)_2$ is nonuniform during the precipitation process, some Ni embryos will grow slower and form the relatively smaller and thinner Ni quasi-hexagonal nanoflakes (Fig. 3(d)).
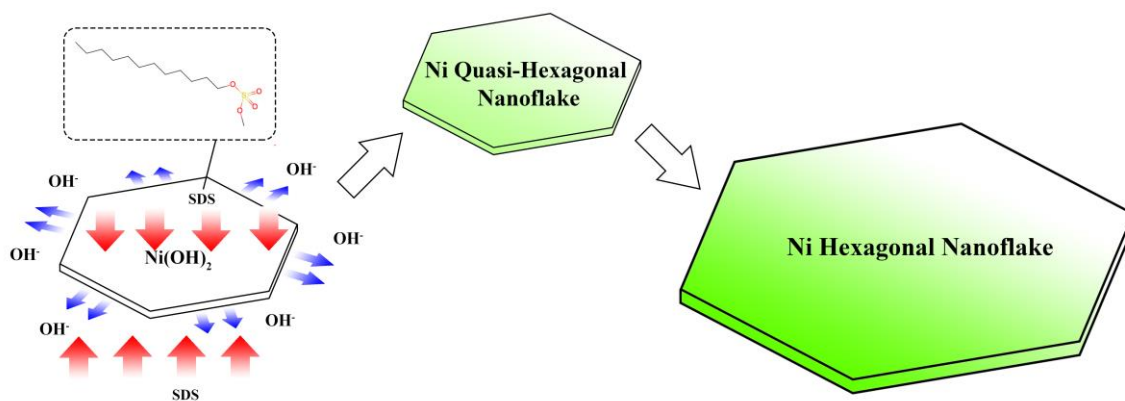

Fig. 7 Schematic diagram of growth mechanism showing the reduction from a $Ni(OH)_2$ flake to a Ni hexagonal nanoflake via a Ni quasi-hexagonal nanoflake.

3.3 Microwave EM properties paraffin-bonded nanoflake composites

The microwave EM properties of the three characteristic types of paraffin-bonded nanoflake composites, namely: R-, V–H-, and H–V-orientated composites, are reported in this section. These include the permeability, permittivity, magnetic and dielectric losses, impedance matching, and microwave EM absorption properties.

3.3.1 Permeability of paraffin-bonded nanoflake composites

Fig. 8(a) and (b) show the measured frequency (f) dependence of the real (μ'_r) and imaginary (μ''_r) parts of the complex relative permeability (μ_r) for the R-, V–H-, and H–V-oriented composites, respectively. The R-oriented composite owns steady μ_r spectra with μ'_r of ~1.1 and μ''_r of ~0.05. The V–H-oriented composite exhibits similar trends in both μ'_r and μ''_r with those of the R-oriented composite, except a slight increment of 3–5% in μ'_r at 1–5.7 GHz (the L, S, and partial C bands), an obvious increment of 40–70% in μ''_r at 1–18 GHz (the whole L–Ku bands), and a small resonance at ~16.2 GHz (in the Ku band). In general, there are four main mechanisms of magnetic loss, including hysteresis loss, domain-wall displacement, eddy-current loss, and natural resonance. First, hysteresis loss mainly results from the time lag of the magnetization vector behind the external EM field vector and can be neglected in weak applied fields or on nanoscale. Second, domain-wall displacement only occurs in multidomain magnetic materials and does not apply to our Ni hexagonal nanoflake magnetic cores with thicknesses (8–15 nm) smaller than a single magnetic domain of Ni (~55 nm). Third, eddy-current loss should be supported by the skin-effect criterion in which $\mu''_r(\mu'_r)^{-2}(f)^{-1}$ should be independent of f. As shown in Fig. 8(c), $\mu''_r(\mu'_r)^{-2}(f)^{-1}$ of our composites is strongly dependent on f and does not fulfill the skin-effect criterion. This is understandable because the 1st SiO_2 insulating dielectric shell can effectively isolate the conductive paths between the Ni hexagonal nanoflake magnetic core and the 2nd PANI conducting dielectric shell in our Ni/SiO_2/PANI hexagonal nanoflakes. Thus, the only possible magnetic loss mechanism that could lead to resonance(s) in the μ_r spectra of our composites is the natural resonance. The H–V-oriented composite demonstrates an obvious increment of 1.8–22.5% in μ'_r at 1–15.5 GHz (the L, S, C, X, and partial Ku bands), a significant increment of 49.1–13919% in μ''_r at 1–18 GHz (the whole L–Ku bands), and a total of four natural resonances at 2.6, 6.6, 15.4, and 16.9 GHz. The enhancement of μ_r in the V–H- and H–V-oriented composites is a result of the interaction between the in-plane [111] easy magnetization (M) of the Ni/SiO_2/PANI hexagonal nanoflakes and the effective

magnetic field vector of incident microwaves [33]. Referring to Fig. 1, the vertical M in the V–H-oriented composite is perpendicular to the magnetic field vector of incident microwaves, which thus has a generally weak response of magnetic moments to incident microwaves. The slight increment in μ_r' and μ_r'' can be ascribed to other in-plane magnetizations possibly parallel to the magnetic field vector. However, for the H–V-oriented composite, the horizontal M is parallel to the magnetic field vector of incident microwaves, which can effectively increase the response of magnetic moments to microwaves and hence μ_r.
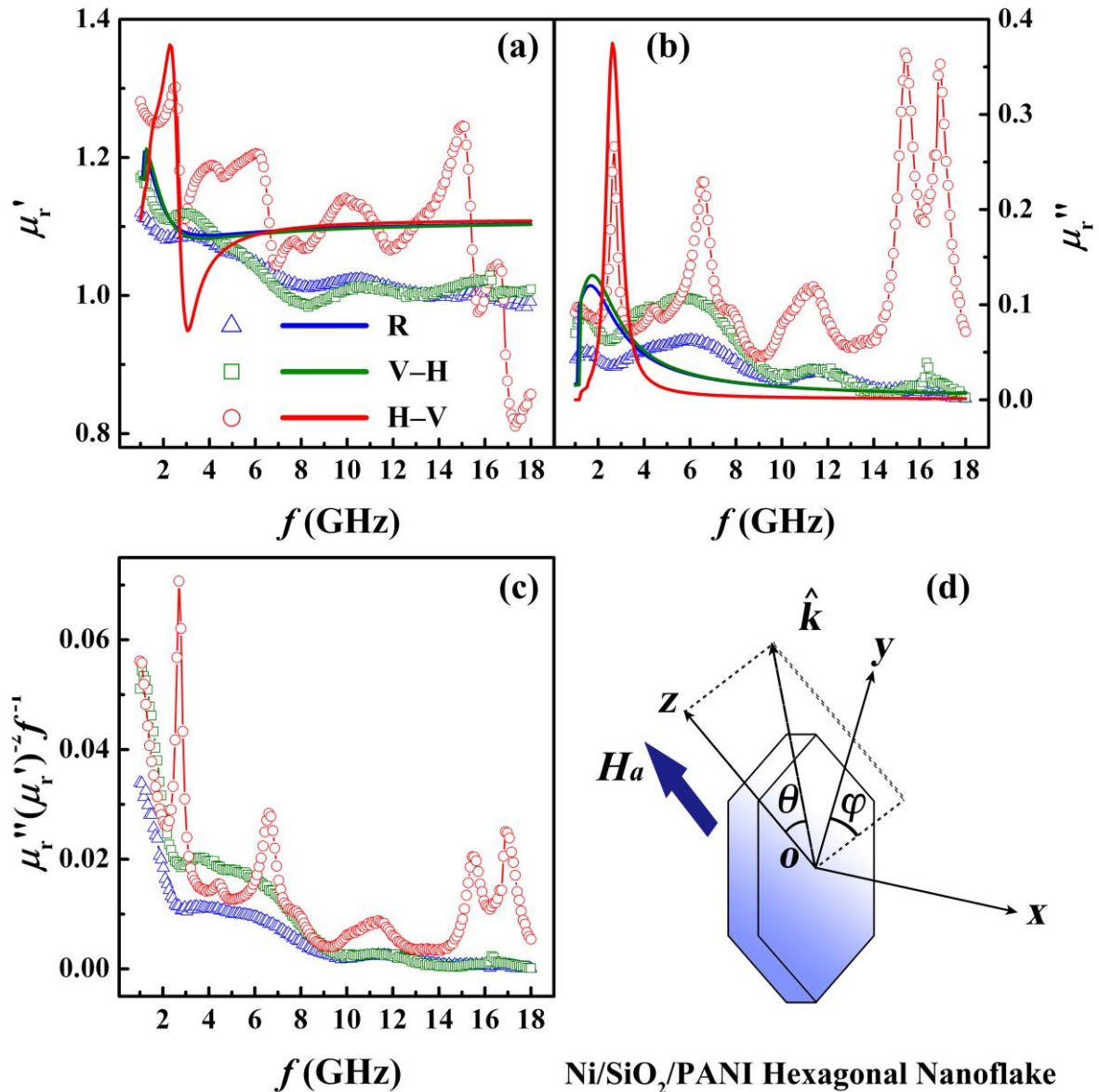

Fig. 8 Measured (line-symbols) and modeled (lines) frequency (f) dependences of (a) real (μ_r') and (b) imaginary (μ_r'') parts of complex relative permeability (μ_r) for R-, V–H-, H–V-oriented composites. (c) Measured f dependence of $\mu_r''(\mu_r')^{-2}f^{-1}$ for the composites. (d) Schematic of Ni/SiO$_2$/PANI hexagonal nanoflakes in the O–XYZ coordinate.

The spectra of solid lines in Figs. 8(a) and 8(b) show the modeled real (μ'_r) and imaginary (μ''_r) parts of the complex relative permeability (μ_r) calculated by the Landau–Lifshitz–Gilbert (LLG) equation and the Bruggeman's effective medium theory (BEMT) for the further study of the easy magnetization orientation-dependent enhancement and resonance in μ_r. In our case, the very thin SiO_2 (7–10 nm) and PANI (13–40 nm) shells are ignored from the calculation. In the simulation, here an O–XYZ coordinate system is adopted to build the model of hexagonal nanoflakes, as shown in the Fig. 8(d). The LLG equation can be described as: [7]

$$\frac{d\boldsymbol{M}}{dt} = -\gamma \boldsymbol{M} \times \boldsymbol{H} + \frac{\alpha}{M_s} \boldsymbol{M} \times \frac{d\boldsymbol{M}}{dt} \tag{3}$$

where $\boldsymbol{M}$ is the magnetization, $\boldsymbol{H}$ is the effective magnetic field including applied static and dynamic fields, anisotropy field, demagnetization field, etc., γ (=2.8 MHz/Oe) is the gyromagnetic ratio, α is the damping coefficient, and M_s is the saturation magnetization. Since the overall magnetization is zero, the applied static field is zero and the demagnetization field is negligible. $\boldsymbol{H}$ in Eq. (3) can be expressed by the applied dynamic field ($\boldsymbol{h}$) perpendicular to $\hat{\boldsymbol{k}}$ as well as the magnetocrystalline anisotropy field (H_a) along the easy magnetization planes of the Ni/SiO$_2$/PANI hexagonal nanoflakes (also the Ni hexagonal nanoflake magnetic core) as follows:

$$\boldsymbol{H} = H_a + \boldsymbol{h}e^{j\omega t - \hat{k}\cdot r} = \left(h_x, -4\pi m_y + h_y, H_a + h_z\right) \tag{4a}$$

$$\boldsymbol{M} = M_s + \boldsymbol{m}e^{j\omega t - \hat{k}\cdot r} = \left(m_x, m_y, M_s + m_z\right) \tag{4b}$$

where H_a represents the only static field counted in our case, M_0 is equal to the saturation magnetization M_s, and ω is the angular frequency. Combining the Maxwell's equations with Eqs. (3) and (4), the permeability tensor can be obtained as follows:

$$\mu = \frac{1}{\varepsilon}\left(\frac{\delta}{j\omega}\right)^2 \begin{bmatrix} 1 - \sin^2\theta\cos^2\theta & -\sin^2\theta\sin\varphi\cos\varphi & -\sin\theta\cos\theta\cos\varphi \\ -\sin^2\theta\sin\varphi\cos\varphi & 1 - \sin^2\theta\cos^2\varphi & -\sin\theta\cos\theta\sin\varphi \\ -\sin\theta\cos\theta\cos\varphi & -\sin\theta\cos\theta\sin\varphi & 1 - \cos^2\theta \end{bmatrix} \tag{5a}$$

$$\delta = j\omega(\mu_0\varepsilon)^{\frac{1}{2}}\left\{\frac{(\mu^2 - \mu - \kappa^2)\sin^2\theta + 2\mu - [(\mu^2 - \mu - \kappa^2)^2\sin^4\theta + 4\kappa^2\cos^2\theta]^{\frac{1}{2}}}{2[(\mu - 1)\sin^2\theta + 1]}\right\}^{\frac{1}{2}} \tag{5b}$$

$$\mu = 1 + \frac{\omega'_0\omega_m}{\omega_0'^2 - \omega^2} \tag{5c}$$

$$\kappa = \frac{-\omega\omega_m}{\omega_0'^2 - \omega^2} \tag{5d}$$

where $\omega_0 = \gamma H_a$, $\omega_m = \gamma 4\pi M_s$, and $\omega_0' = \omega_0 + j\omega\alpha$. The eigenvalues of the permeability tensors are the intrinsic permeability (μ_i). For the R-oriented composite, 10,000 sets of θ and φ are randomly generated to calculate an equivalent average permeability tensor using Eq. (5). For the V–H- and H–V-oriented composites, $\theta=0$ and $\theta=\pi/2$ are adopted, respectively, to determine the permeability tensor because M is along the DC magnetic alignment field (H) as shown in Fig. 1. However, as the 2D planes are random in the azimuth angle as shown in the V–H- and H–V-oriented composites in Fig. 1, the φ angle is randomly generated with 10,000 sets. The final effective permeability (μ_{eff}) of the composites is obtained using the BEMT [34],

$$p\frac{\mu_i - \mu_{\text{eff}}}{\mu_i + 2\mu_{\text{eff}}} + (1-p)\frac{\mu_m - \mu_{\text{eff}}}{\mu_m + 2\mu_{\text{eff}}} = 0 \qquad (6)$$

where p is the volume fraction of Ni hexagonal nanoflakes and μ_m (=1) is the permeability of paraffin.

M_s of the Ni hexagonal nanoflakes is measured to be 32.5 emu/g. H_a of 3.5 kOe and α of 0.9, 0.8, and 0.1 are used in the modeling of the R-, V–H-, H–V-oriented composites, respectively. As shown in Fig. 8(a) and (b), the modeled μ_r' and μ_r'' spectra (lines) agree well with the measured μ_r' and μ_r'' ones (line-symbols) in the L–S band for the composites with R, V–H, and H–V orientations, and the obvious resonances are revealed at 1.4, 1.5, and 2.7 GHz, respectively. However, the other resonances are not predicted in the μ_r' and μ_r'' spectra of the H–V-oriented composite since these resonances may be induced by the natural resonances of other in-plane magnetizations in practice.

3.3.2 Permittivity of paraffin-bonded nanoflake composites

The measured frequency (f) dependence of the real (ε_r') and imaginary (ε_r'') parts of the complex relative permittivity (ε_r) of the R-, V–H-, and H–V-oriented composites are shown in Fig. 9(a) and (b), respectively. Comparing to the ε_r' spectrum of the R-oriented composite, the V–H-oriented composite has an increment of ~25%, while the H–V-oriented one has a decrement of ~10%. As ε_r' mainly depends on the effective polarization capacity, the interfacial polarization (P) of the core/shell/shell structure of the Ni/SiO$_2$/PANI hexagonal nanoflakes (Fig. 1) should play an important role. For such a 2D Ni/SiO$_2$/PANI hexagonal nanoflake, most of the P should be perpendicular to its two major hexagonal surfaces. For the V–H-oriented composite, P in the polar coordinate plane (Fig. 1) is effective because it is parallel to the effective electric field vector of incident microwaves. For the H–V-orientated composite, P is random to the electric field vector (Fig. 1) that leads to a weak ε_r'. The V–H

orientation of the Ni/SiO$_2$/PANI hexagonal nanoflakes also improves ε_r'' with an increment of 50–80%. The H–V-oriented composite has ε_r'' similar to the R-oriented one. However, a strong polarization is seen at ~17 GHz in all the R-, V–H-, and H–V-oriented composites. The Cole-Cole plots of the R-, V–H-, and H–V-oriented composites are shown in Fig. 9(c) based on the measured ε_r' and ε_r'' spectra in Fig. 9(a) and (b). Accordingly to the Debye's polarization theory described by:

$$(\varepsilon_r' - \varepsilon_\infty)^2 + (\varepsilon_r'')^2 = (\varepsilon_s - \varepsilon_\infty)^2 \tag{7}$$

where ε_∞ and ε_s are the optical dielectric constant and the stationary dielectric constant, respectively [35], the obvious semicircles observed in all the R-, V–H-, and H–V-oriented composites indicate a Debye dipolar polarization at ~17 GHz. This Debye dipolar polarization should be the intrinsic polarization (P_I) of the Ni hexagonal nanoflake magnetic cores (Fig. 1) because the electronic, ionic, and atomic polarizations are negligible at microwave frequencies. Comparing to the R- and V–H-oriented composites, the in-plane P_I of the Ni hexagonal nanoflake magnetic cores have more chances to get parallel with the electric field vector in the H–V-oriented composites so that its Debye dipolar polarization is enhanced.
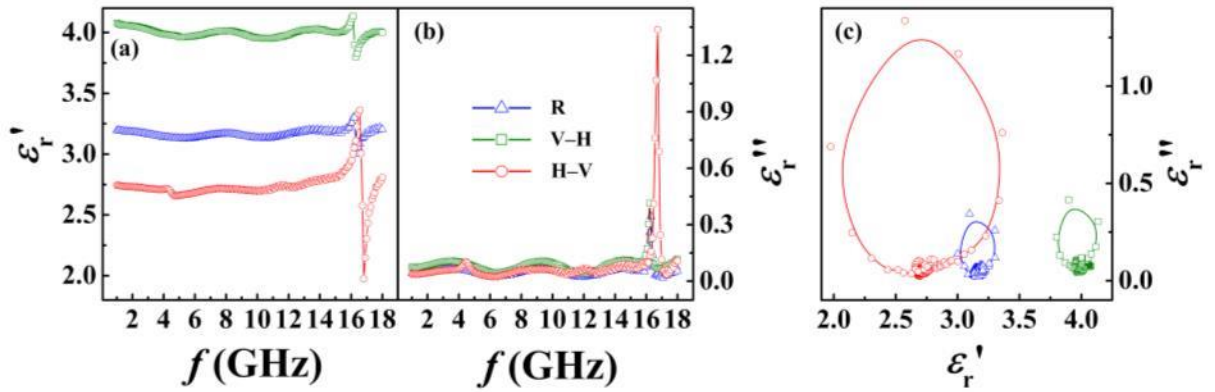

Fig. 9 Measured frequency (f) dependence of (a) real (ε_r') and (b) imaginary (ε_r'') parts of complex relative permittivity (ε_r) for R-, V–H-, H–V-oriented composites. (c) Cole-Cole plots for the composites based on (a) and (b).

3.3.3 Magnetic and dielectric losses of paraffin-bonded nanoflake composites

Fig. 10(a) and (b) show the magnetic loss tangent ($\tan\delta_\mu = \mu_r''/\mu_r'$) and dielectric loss tangent ($\tan\delta_\varepsilon = \varepsilon_r''/\varepsilon_r'$) spectra of the R-, V–H-, and H–V-oriented composites, respectively. The $\tan\delta_\mu$ spectra are calculated using the measured μ_r' and μ_r'' spectra in Fig. 8(a) and (b), while the $\tan\delta_\varepsilon$ spectra are calculated using the measured ε_r' and ε_r'' spectra in Fig. 9(a) and

(b). For the $\tan\delta_\mu$ spectra in Fig. 10(a), the V–H-oriented composite has a relatively obvious enhancement in $\tan\delta_\mu$ at 1–8 GHz (the L, S, and C bands) in comparison with the R-oriented one. Interestingly, the H–V-oriented composite has a significant enhancement in $\tan\delta_\mu$ at 9–18 GHz (the X and Ku bands) because the horizontal orientation of the in-plane M of the Ni/SiO$_2$/PANI hexagonal nanoflakes in the H–V-oriented composite is parallel to the effective magnetic field vector of incident microwaves (Fig. 1). For the $\tan\delta_\varepsilon$ spectra in Fig. 10(b), the V–H-oriented composite has a much higher $\tan\delta_\varepsilon$ almost throughout the whole f range, except at 4.5, 12, and 17 GHz, when compared with the R- and H–V-oriented composites. The reason can be explained by the horizontal orientation of the out-of-plane P of the Ni/SiO$_2$/PANI hexagonal nanoflakes in the V–H-oriented composite to be parallel to the effective electric field vector of incident microwaves (Fig. 1).

In addition to the contribution to the orthogonal M and P design in our Ni/SiO$_2$/PANI hexagonal nanoflakes, we have also utilized the 1st SiO$_2$ insulating dielectric shell to achieve a better EM impedance matching in the Ni/SiO$_2$/PANI hexagonal nanoflakes. That is, as the Ni hexagonal nanoflake magnetic core and the 2nd PANI conducting dielectric shell have very high ε_r, their resulting high ε_r is unable to establish an effective EM impedance matching with the limited μ_r in the Ni hexagonal nanoflake magnetic core. Thus, an intermediate SiO$_2$ insulating dielectric shell is introduced to isolate the conducting Ni hexagonal nanoflake magnetic core from the PANI conducting dielectric shell, to minimize the eddy-current loss, and to reduce the excessive ε_r and $\tan\delta_\varepsilon$ due to the Ni hexagonal nanoflake magnetic core and the PANI conducting dielectric shell, for a better EM impedance matching.
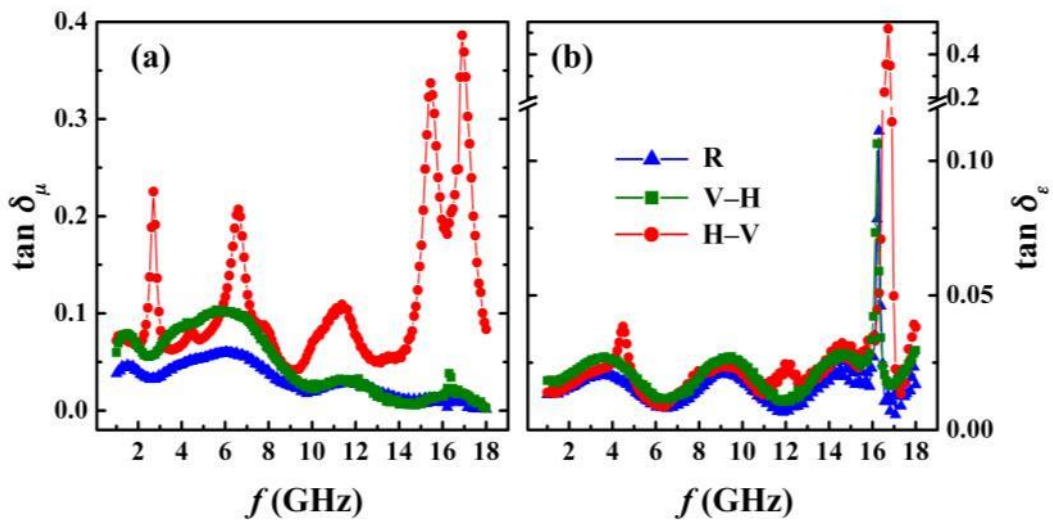

Fig. 10 (a) Magnetic loss tangent ($\tan\delta_\mu$) (b) dielectric loss tangent ($\tan\delta_\varepsilon$) spectra of R-, V–H-, and H–V-oriented composites.

3.3.4 Impedance matching in paraffin-bonded nanoflake composites

To achieve a perfect impedance matching, Z_{in} has to be unity in Eq. (2) such that RL becomes negative infinity in Eq. (1) for a total absorption of incident microwaves. Accordingly, the six control parameters (i.e., μ_r', μ_r'', ε_r', ε_r'', f, and d) have to be considered simultaneously in the impedance matching design. The solid lines in Fig. 11 give the calculated impedance matching maps of the R-, V–H-, and H–V-oriented composites. These solid lines are determined under the objective of obtaining the perfect impedance matching condition of Z_{in}=1 in Eq. (2) by using the six control parameters. Here, we put μ_r' and μ_r'' as the x-axis and y-axis variables, respectively, to form two interrelated groups of μ_r''–μ_r' curves, including the purple one at various d/λ (where λ=c/f) and the light blue one at various ε_r', by setting μ_r', μ_r'', d/λ, and ε_r' at the practically viable ranges of 0.6–1.4, 0–0.4, 0.05–0.1, and 2–4, respectively, in accordance with Figs. 8 and 9. The value of ε_r'' is approximated by an average $\tan\delta_\varepsilon$ (=$\varepsilon_r''/\varepsilon_r'$) of 0.022 from Fig. 10. It can be seen from Fig. 11 that there are three crossing points for the two interrelated groups of the calculated μ_r''–μ_r' curves as highlighted by blue crossmarks. These include the 1st one crossed at d/λ=0.07 and ε_r'=2, the 2nd one crossed at d/λ=0.05 and ε_r'=3, and the 3rd one crossed d/λ=0.05 and ε_r'=4. These three crossing points elucidate the existence of three possible cases for perfect impedance matching in absorbers. Table I summarizes the control parameters of these three crossing points. Thus, Fig. 11 can be used as a design guiding map for perfect impedance matching in absorbers.

The symbol-lines in Fig. 11 plot the measured μ_r''–μ_r' curves of the R-, V–H-, and H–V-oriented composites using the measured μ_r' and μ_r'' spectra in Fig. 8(a) and (b). It is clear that the measured μ_r''–μ_r' curve of the H–V-oriented composite is the most closest to, and even has a large overlapping portion with, the two interrelated groups of the calculated μ_r''–μ_r' curves. This indicates the highest chance of achieving a perfect impedance matching in the H–V-oriented composite in comparison with the R- and V–H-oriented composites. Importantly, the measured μ_r''–μ_r' curve of the H–V-oriented composite have a better overlap with the 2nd (d/λ=0.05, ε_r'=3) and 3rd (d/λ=0.05, ε_r'=4) crossing points than the 1st one (d/λ=0.07, ε_r'=2). This suggests that the 2nd and 3rd crossing points are more referenceable to achieve a good impedance matching in our H–V-oriented composite. Table II summarizes the measured control parameters that are capable of achieving the best impedance matching in our H–V-oriented composite with reference to the 2nd and 3rd crossing points. Thus, we are expected to have two strong absorption cases: one at f=15.4 GHz and d=9.7 mm, while the other one at f=17.4 GHz and d=8.6 mm, by referencing to the 2nd and 3rd crossing points, respectively, in

our H–V-oriented composite. More details will be described in microwave EM absorption in Section 3.3.5.
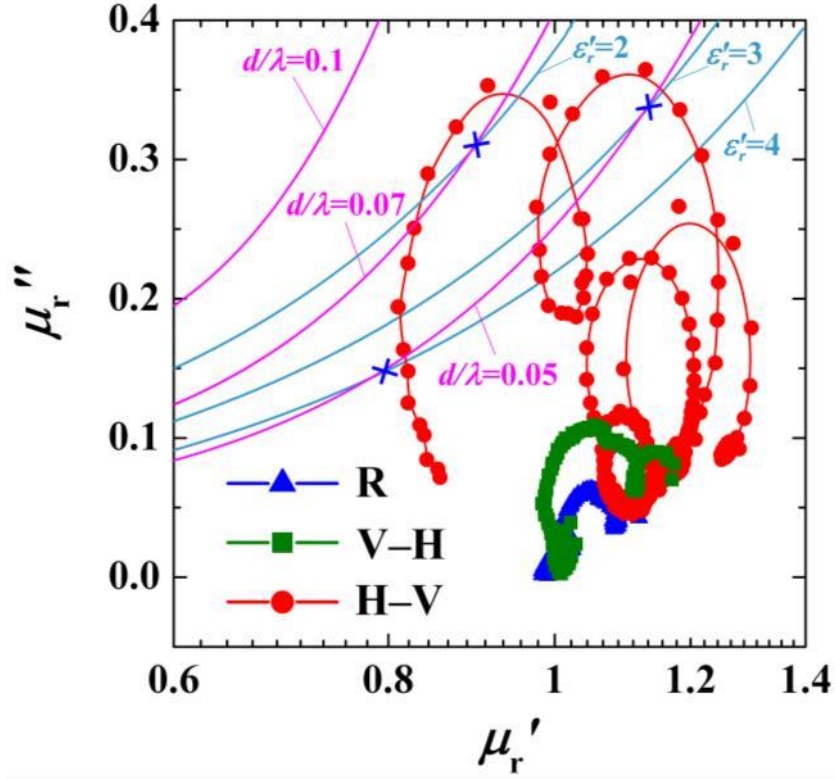

Fig. 11 Calculated impedance matching maps (lines) of R-, V–H-, and H–V-oriented composites. The symbol-lines are measured μ_r''–μ_r' curves based on the measured μ_r' and μ_r'' spectra in Fig. 8(a) and (b).

Table I Calculated control parameters of three crossing points possible for perfect impedance matching in absorbers.

Crossing Point	μ_r'	μ_r''	ε_r'	ε_r''	d/λ
1 (d/λ=0.07; ε_r'=2)	0.892	0.304	2	0.044	0.07
2 (d/λ=0.05; ε_r'=3)	1.127	0.333	3	0.066	0.05
3 (d/λ=0.05; ε_r'=4)	0.790	0.146	4	0.088	0.05

Table II Measured control parameters that are capable of achieving the best impedance matching in H–V-oriented composite with reference to the 2nd and 3rd crossing points in Table I.

Referencing to Crossing Point	μ_r'	μ_r''	ε_r'	ε_r''	f (GHz)	d (mm)	f_{RL} (GHz)	d_{RL} (mm)	RL (dB)
2	1.155	0.349	3	0.066	15.4	9.7	15.4	7.8	-38.4
3	0.815	0.157	4	0.088	17.4	8.6	17.2	8.7	-41.5

3.3.5 Microwave EM absorption of paraffin-bonded nanoflake composites

Fig. 12 shows the 2D-contour plots of the frequency (f) and thickness (d) dependences on reflection loss (RL) (in the upper row) as well as the f dependence of RL at various d (in the lower row) for the R-, V–H-, and H–V-oriented composites. The relation of RL–f–d is calculated using the measured μ_r (Fig. 8) and ε_r (Fig. 9) spectra at different d in Eqs. (1) and (2). Comparing to the R-oriented composite, the V–H- and H–V-oriented composites have enhanced RL in the L–Ku bands. It is especially significant for the H–V-oriented composite having a broad absorbing bandwidth (RL<–5 dB) of 4 GHz and a wide d range of 7–10 mm. Two absorbing bands of very large negative RL is found for -38.4 dB at f=15.4 GHz and d=7.8 mm, and for –41.5 dB at f=17.4 GHz and d=8.7 mm. These f and d values agree well with the predicted values with reference to the 2nd and 3rd crossing points in Table II. Moreover, the steady absorption in the Ku (12–18 GHz) band for d varying between 2–10 mm is achieved. The absorbing band is not sensitive to the variation of d in the H–V-oriented composite because of the improved EM impedance matching as discussed in Section 3.3.4.
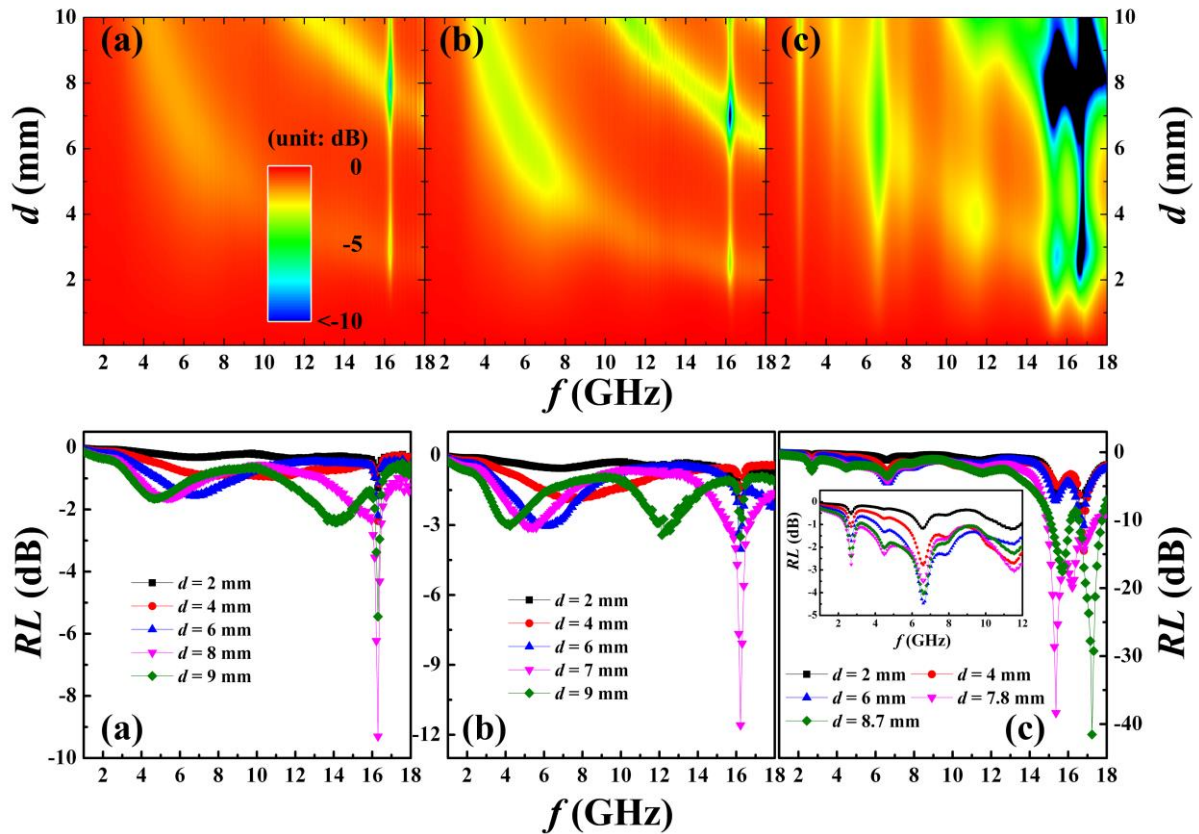

Fig. 12 2D-contour plots of frequency (f) and thickness (d) dependences on reflection loss (RL) (upper) and f dependence of RL at various d (lower) for (a) R-, (b) V–H-, and (c) H–V-oriented composites.

4. Conclusion

We have designed and synthesized core/shell/shell-structured Ni/SiO$_2$/PANI hexagonal nanoflakes to exhibit orthogonal in-plane M and P_I as well as out-of-plane P using a three-step liquid chemical method. The physicochemical properties of the nanoflakes have been studied and a growth mechanism has been proposed. Three characteristic types of paraffin-bonded, ring-shaped nanoflake composites have been fabricated to exhibit R, V–H, and H–V orientations of the orthogonal M and P to their two major surfaces through a magnetic alignment and thermal curing process. The effect of directional orientation of the orthogonal M and P on the microwave EM properties has been evaluated experimentally and theoretically in the L–Ku (1–18 GHz) bands of microwaves. The major focus has been paid to investigate the orientation effect of the orthogonal M and P on the microwave EM properties of the composites. The in-plane M parallel to the effective magnetic field vector of incident microwaves in the H–V-oriented composite results in a significant enhancement in permeability with multiple natural resonances in the whole L–Ku bands in comparison with the V–H- and R-oriented composites. The out-of-plane P parallel to the effective electric field vector of incident microwaves in the V–H-oriented composite leads to an obvious improvement in permittivity compared to the R- and H–V-oriented composites. Theoretical predictions have been established using the Landau–Lifshitz–Gilbert equation and the Bruggeman's effective medium theory for permeability and the Debye's polarization theory for permittivity. The best microwave EM impedance matching and absorption has been achieved in the H–V-oriented composite, showing a broad absorbing bandwidth of 4 GHz, a wide absorber thickness range of 7–10 mm, and the minimal RL of -41.5 dB in the Ku (12–18 GHz) band.

Author Contributions:

Jiaheng Wang performed both the theoretical and experimental work. Siu Wing Or conceived the project and guided Jiaheng Wang and Jun Tan in the whole work. Jun Tan provided support in HRTEM, SAED, and FFT evaluations using STEM.

References

[1]   L.B. Kong, Z.W. Li, L. Liu, R. Huang, M. Abshinova, Z.H. Yang, C.B. Tang, P.K. Tan, C.R. Deng, S. Matitsine, Recent progress in some composite materials and structures for specific electromagnetic applications, International Materials Reviews 58(4) (2013) 203–259.

[2]   F. Qin, C. Brosseau, A review and analysis of microwave absorption in polymer composites filled with carbonaceous particles, Journal of Applied Physics 111(6) (2012) 061301.

[3]   H. Wang, Y. Dai, W. Gong, D. Geng, S. Ma, D. Li, W. Liu, Z. Zhang, Broadband microwave absorption of CoNi@C nanocapsules enhanced by dual dielectric relaxation and multiple magnetic resonances, Applied Physics Letters 102(22) (2013) 223113.

[4]   Q. Liu, Q. Cao, H. Bi, C. Liang, K. Yuan, W. She, Y. Yang, R. Che, CoNi@SiO$_2$@TiO$_2$ and CoNi@Air@TiO$_2$ microspheres with strong wideband microwave absorption, Advanced Materials 28(3) (2016) 486–490.

[5]   X. Liu, S. Wing Or, C.M. Leung, S.L. Ho, Core/shell/shell-structured nickel/carbon/polyaniline nanocapsules with large absorbing bandwidth and absorber thickness range, Journal of Applied Physics 115(17) (2014) 053115.

[6]   J. Wang, S.W. Or, C.M. Leung, Effect of shell permutation on electromagnetic properties of ZnFe$_2$O$_4$/(PANI, SiO$_2$) core/double-shell nanostructured disks, Journal of Applied Physics 117(17) (2015) 17A505.

[7]   J. Wang, S.W. Or, Orientation-induced enhancement in electromagnetic properties of ZnFe$_2$O$_4$/SiO$_2$/PANI core/shell/shell nanostructured disks, AIP advances 6(5) (2016) 055908.

[8]   L. Yan, J. Wang, X. Han, Y. Ren, Q. Liu, F. Li, Enhanced microwave absorption of Fe nanoflakes after coating with SiO$_2$ nanoshell, Nanotechnology 21(9) (2010) 095708.

[9]   M. Fu, Q. Jiao, Y. Zhao, Preparation of NiFe$_2$O$_4$ nanorod–graphene composites via an ionic liquid assisted one-step hydrothermal approach and their microwave absorbing properties, Journal of Materials Chemistry A 1(18) (2013) 5577–5586.

[10] Y. Yang, C. Xu, Y. Xia, T. Wang, F. Li, Synthesis and microwave absorption properties of FeCo nanoplates, Journal of Alloys & Compounds 493(1–2) (2010) 549–552.

[11] X.L. Dong, X.F. Zhang, H. Huang, F. Zuo, Enhanced Microwave Absorption in Ni/Polyaniline Nanocomposites by Dual Dielectric Relaxations, Applied Physics Letters 92(1) (2008) 301.

[12] J. Wang, P. Zhu, J. Wang, S.W. Or, S. Ho, J. Tan, Interchange core/shell assembly of diluted magnetic semiconductor CeO_2 and ferromagnetic ferrite Fe_3O_4 for microwave absorption, AIP Advances 7(5) (2017) 055811.

[13] L. Wang, Y. Huang, X. Sun, H. Huang, P. Liu, M. Zong, Y. Wang, Synthesis and microwave absorption enhancement of graphene@Fe_3O_4@SiO_2@NiO nanosheet hierarchical structures, Nanoscale 6(6) (2014) 3157.

[14] J. Villain, Theory of one- and two-dimensional magnets with an easy magnetization plane. II. The planar, classical, two-dimensional magnet, Journal De Physique, 36(6) (1975) 581-590.

[15] P. Misra, Y. J. Sun, O. Brandt, H. T. Grahn, In-plane polarization anisotropy and polarization rotation for M-plane GaN films on $LiAlO_2$, Applied Physics Letters, 83(21) (2003) 4327-4329.

[16] R. Han, X. H. Han, L. Qiao, T. Wang, F. S. Li, Enhanced microwave absorption of ZnO-coated planar anisotropy carbonyl-iron particles in quasimicrowave frequency band, Materials Chemistry and Physics, 128(3) (2011) 317-322.

[17] R. Xu, T. Xie, Y. Zhao, Y. Li, Single-crystal metal nanoplatelets: cobalt, nickel, copper, and silver, Crystal Growth & Design, 7(9) (2007) 1904–1911.

[18] W. Stöber, A. Fink, E. Bohn, Controlled growth of monodisperse silica spheres in the micron size range, Journal of Colloid and Interface Science, 26(1) (1968) 62-69.

[19] W. Li, D. Y. Zhao, Extension of the Stöber Method to Construct Mesoporous SiO_2 and TiO_2 Shells for Uniform Multifunctional Core–Shell Structures, Advanced Materials, 25 (2013) 142-149.

[20] X. L. Dong, X. F. Zhang, H. Huang, F. Zuo, Enhanced Microwave Absorption in Ni/Polyaniline Nanocomposites by Dual Dielectric Relaxations, Applied Physics Letters, 92(1) (2008) 301.

[21] A. M. Nicolson, G. F. Ross, Measurement of the intrinsic properties of materials by time-domain techniques, IEEE Transactions on Instrumentation Measurement, IM-19(4) (1970) 377-382.

[22] W. B. Weir, Automatic measurement of complex dielectric constant and permeability at microwave frequencies, Proceeding of the IEEE, 62(1) (1974) 33-36.

[23] C.D. Wanger, W.M. Riggs, L.E. Davis, J.F. Moulder, G.E. Muilenberg, Handbook of X-ray Photoelectron Spectroscopy, Physical Electronics Division, Perkin-Elmer Corp., USA, 1979.

[24] C. Tang, Y. Liu, C. Xu, J. Zhu, X. Wei, L. Zhou, L. He, W. Yang, L. Mai, Ultrafine Nickel-Nanoparticle-Enabled SiO_2 Hierarchical Hollow Spheres for High-Performance Lithium Storage, Advanced Functional Materials 28(3) (2018) 1704561.

[25] Ö. Yavuz, M.K. Ram, M. Aldissi, P. Poddarb, S. Hariharanb, Synthesis and the physical properties of MnZn ferrite and NiMnZn ferrite–polyaniline nanocomposite particles, Journal of Materials Chemistry 15 (2005) 810-817.

[26] T.C. Girija, M.V. Sangaranarayanan, Analysis of polyaniline-based nickel electrodes for electrochemical supercapacitors, Journal of Power Sources 156(2) (2006) 705-711.

[27] Y. Furukawa, F. Ueda, Y, Hyodo, I. Harada, T. Nakajima, T. Kawagoe. Vibrational spectra and structure of polyaniline. Macromolecules 21(5) (1988) 1297-1305.

[28] G. Louarn, M. Lapkowski, S. Quillard, A. Pron, J. P. Buisson, S. Lefrant, Vibrational Properties of PolyanilineIsotope Effects, The Journal of Physical Chemistry 100(17) (1996) 6998-7006.

[29] I.S. Lee, N. Lee, J. Park, B.H. Kim, Y.-W. Yi, T. Kim, T.K. Kim, I.H. Lee, S.R. Paik, T. Hyeon, Ni/NiO core/shell nanoparticles for selective binding and magnetic separation of histidine-tagged proteins, Journal of the American Chemical Society 128(33) (2006) 10658–10659.

[30] T. Liu, Y. Pang, M. Zhu, S. Kobayashi, Microporous Co@CoO nanoparticles with superior microwave absorption properties, Nanoscale 6(4) (2014) 2447–2454.

[31] H. Wang, H.S. Casalongue, Y. Liang, H. Dai, $Ni(OH)_2$ nanoplates grown on graphene as advanced electrochemical pseudocapacitor materials, Journal of the American Chemical Society 132(21) (2010) 7472–7477.

[32] S. Jiang, R. Guo, Effect of polyester fabric through electroless Ni-P plating, Fibers and polymers 9(6) (2008) 755–760.

[33] W. Chen, M. Han, L. Deng, High frequency microwave absorbing properties of cobalt nanowires with transverse magnetocrystalline anisotropy, Physica B Condensed Matter 405(6) (2010) 1484–1488.

[34] J. Jiang, D. Li, D. Geng, J. An, J. He, W. Liu, Z. Zhang, Microwave absorption properties of core double-shell $FeCo/C/BaTiO_3$ nanocomposites, Nanoscale 6(8) (2014) 3967.

[35] X. Zhang, X. Dong, H. Huang, Y. Liu, W. Wang, X. Zhu, B. Lv, J. Lei, C. Lee, Microwave absorption properties of the carbon-coated nickel nanocapsules, Applied Physics Letters 89(5) (2006) 053115.